

Surface engineering on bulk Cu₂O for efficient electrosynthesis of urea

Received: 12 July 2023

Accepted: 27 February 2025

Published online: 05 April 2025

Zechuan Dai^{1,2}, Yanxu Chen^{1,2}, Huaikun Zhang¹, Mingyu Cheng¹, Bocheng Zhang¹, Pingyi Feng¹, Yafei Feng¹ & Genqiang Zhang¹✉

Electrochemical urea synthesis has recently emerged as a fascinating energy-efficient alternative route, while it remains challenging to achieve simultaneously high production rate and Faradaic efficiency. Herein, we realize an energy-favorable electrochemical C–N coupling path through CO₂ and NO₃[−] co-reduction at the heterointerfaces of Cu/Cu₂O microparticles, generated by in-situ electrochemical engineering on bulk Cu₂O. We achieve urea production rate of 632.1 μg h^{−1}mg_{cat.}^{−1} with a corresponding Faradaic efficiency of 42.3% at −0.3 V (versus RHE) under ambient conditions. Operando synchrotron radiation-Fourier transform infrared spectroscopy, along with theoretical calculations, reveals the coupling of intermediates NOH* and CO* at the heterointerfaces, benefiting from the modified electronic structure. This work provides a practical route for catalyst design and insights into urea electrosynthesis systems.

Urea (CO(CH₂)₂) as one of the most significant nitrogen fertilizers, not only serves as agricultural product to meet the needs of the growing population, but also the industrial chemical feedstock to manufacture various chemicals^{1,2}. Conventionally, urea synthesis is conducted by Haber–Bosch and Bosch–Meiser processes containing two consecutive reaction steps (N₂ + H₂ → NH₃; NH₃ + CO₂ → CO(NH₂)₂), which require harsh conditions (150–200 °C, 150–250 bar) with more than 2% of global energy consumption^{3–5}. Compared with the conventional approach, the electrochemical C–N coupling approach using CO₂ and the available nitrogen sources (N₂ and NO_x[−]) in daily life is a “kill two-bird with one stone” decision for urea production featuring reactant sustainability and the overall energy efficiency, where some pioneering progresses have been achieved^{6–12}. Very recently, Wang et al. reported a urea electrosynthesis strategy by using N₂ and CO₂ as reactants with a yield rate of 0.024 μmol cm^{−2} h^{−1} and faradaic efficiency (FE) of 0.66% using PdCu nanoparticle anchored on TiO₂ nanosheets⁶. Moreover, Zhang et al. reported the vacancy-rich ZnO porous nanosheets which realize electrosynthesis of urea from NO₂[−] and CO₂ with a higher FEs (23.26%)⁷. Although these inspiring breakthroughs, it remains grand challenge to achieve “all-round high” (high urea yield rate, FE, selectivity and stability) for urea electrosynthesis owing to the limitations of

ideal electrocatalysts^{13–18}. More importantly, the development of unique C–N coupling path is still at the infant stage, where much input should be devoted in order to provide protocols for catalyst design, aiming to achieve efficient and cost-effective urea electrosynthesis.

Copper-based materials have been developed as a family of catalysts for CO₂RR to generate multi-carbon products upon niche control over the real active sites for C–C coupling^{19–24}. Very recently, some pioneering work demonstrated the possibility to activate the C–N coupling capability of Cu-based catalysts for urea electrosynthesis by engineering its electronic structure^{25–31}. For example, Wang et al. reported that the Cu single atoms can be utilized for electrocatalytic urea synthesis upon the coupling of CO* and NO* intermediates, achieving a yield rate of 52.84 mmol h^{−1}g_{cat.}^{−1} at −1.6 V with the Faradaic efficiency of 3.42%²⁵. Subsequently, Pan et al. disclosed that constructing Pd₁Cu₁ dual-atom catalyst can effectively enhance the yield rate to 166.67 mol_{urea}mol_{Pd}^{−1} h^{−1} with a higher Faradaic efficiency of 22.54% upon a distinctive C–N coupling path (N₂* and CO*)²⁶. These results stimulated the unremitting dedication to explore more efficient C–N coupling path by engineering Cu based catalyst in order to further push the limits of yield rate and FE for urea electrosynthesis. The major bottleneck issues in current stage include: (i) The exploration of

¹Hefei National Research Center for Physical Sciences at the Microscale, CAS Key Laboratory of Materials for Energy Conversion Department of Materials Science and Engineering, University of Science and Technology of China, 230026 Hefei, Anhui, China. ²These authors contributed equally: Zechuan Dai, Yanxu Chen. ✉e-mail: gqzhangmse@ustc.edu.cn

scalable yet cost-effective strategy for active sites manipulation in Cu-based catalysts to activate unique yet energy favorable C–N coupling path; (ii) The systematic yet in-depth investigation on the underlying catalytic mechanism in order to generate protocol for future development; (iii) The proof-of-concept demonstration for the practicability on the urea electrosynthesis in two-electrode system.

Herein, we discovered a unique C–N coupling pathway of CO^* and NOH^* intermediates for urea electrosynthesis achieved by constructing Cu/Cu₂O heterointerfaces through in situ electrochemical reduction of bulk Cu₂O, where all-round high electrochemical performance, i.e. an average yield rate of $632.1 \mu\text{g h}^{-1} \text{mg}_{\text{cat}}^{-1}$ at -0.3 V (versus RHE), as well as high FE of 42.3%, nitrogen selectivity ($N_{\text{urea}}\text{-selectivity}$) and carbon selectivity ($C_{\text{urea}}\text{-selectivity}$) of $\sim 70\%$. Utilizing Operando synchrotron radiation-Fourier transform infrared spectroscopy (SR-FTIR) and in situ Raman spectroscopy, we revealed the formation of C–N chemical bonds and elucidated the dynamic changes of C and N intermediate species during the electrochemical coupling cascade for urea synthesis. Specifically, it is suggested that the h-Cu/Cu₂O MPs was effective for the formation of NOH^* intermediates, resulting in a large quantity of NOH^* and CO^* intermediates at the Cu/Cu₂O heterointerface, which also acts as C–N coupling active sites, leading to an low

energy barrier for urea formation. Density functional theory (DFT) calculations show that the electron transfer at the Cu/Cu₂O hetero-interfaces not only produces more thermally neutral bond free energies (ΔG_{H}^*) but also forms unique C–N active sites, compared to pure Cu or Cu₂O. As a proof-of-concept demonstration for practicability, the two-electrode system coupled with hydrazine oxidation reaction (HzOR) can improve the overall current up to ~ 10 times (from 5 to 50 mA cm^{-2})^{32–35}, leading to an increased cathodic urea yield up to $883.6 \mu\text{g h}^{-1} \text{mg}_{\text{cat}}^{-1}$.

Results and discussion

Primarily, we prepared h-Cu/Cu₂O MPs via electrochemical reduction of commercial bulk Cu₂O particles with average sizes of $2 \mu\text{m}$ (Supplementary Fig. 1). The electrochemical reduction conditions involve the reduction of bulk Cu₂O material at -1.5 V versus RHE for 1200 s. The X-ray diffraction (XRD) pattern of the samples (Fig. 1a) ensures the co-existence of both Cu (JCPDS No. 89-2838) and Cu₂O (JCPDS No. 05-0667) phases after electrochemical reduction process, implying the formation of h-Cu/Cu₂O MPs. The morphology of h-Cu/Cu₂O MPs (Supplementary Fig. 2) exhibits no obvious variation compared with that of bulk Cu₂O (Supplementary Fig. 3). However, high-resolution

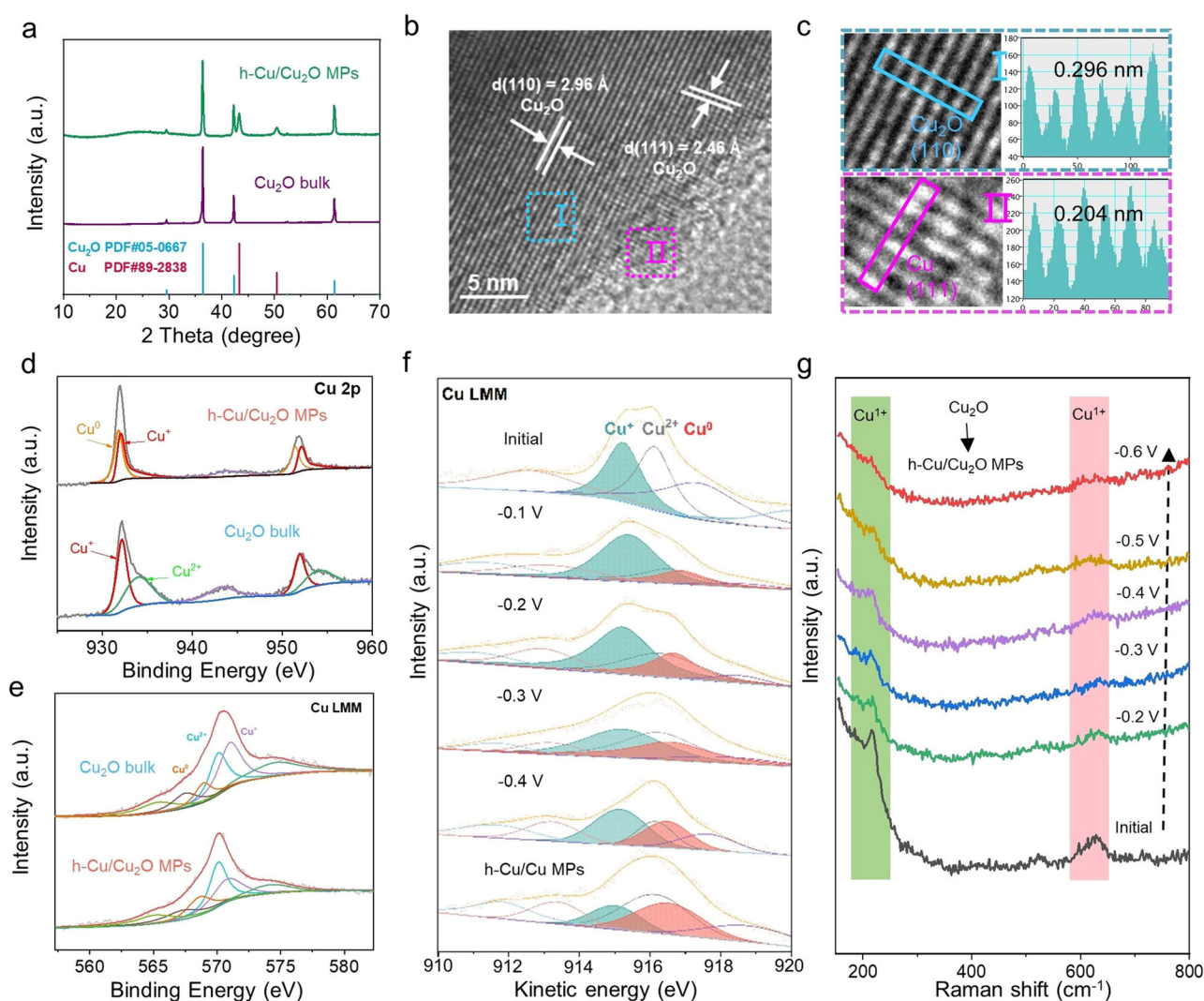


Fig. 1 | Morphological and structural characterizations of the h-Cu/Cu₂O MPs. **a** XRD patterns of h-Cu/Cu₂O MPs and bulk Cu₂O. **b**, **c** HRTEM images of h-Cu/Cu₂O MPs. **d** XPS spectra of Cu 2p of Cu₂O and h-Cu/Cu₂O MPs. **e** Cu LMM AES spectra of Cu₂O and h-Cu/Cu₂O MPs. Potential-dependent (f) in situ XPS curves of Cu LMM

AES spectra of bulk Cu₂O under electrochemical reduction. **(g)** in situ electrochemical Raman spectra of bulk Cu₂O under electrochemical reduction. Source data for Fig. 1 are provided as a Source Data file.

transmission electron microscopy (HRTEM) analysis (Fig. 1b) provides direct evidence for the formation of Cu/Cu₂O heterointerfaces at the surface, where the spacing of lattice fringes of 0.204 nm can be indexed to (111) planes of Cu phase (Fig. 1c), which is consistent with selected-area electron diffraction (SAED) patterns (Supplementary Figs. 4, 5). The high-angle annular dark-field scanning TEM (HAADF-STEM) and energy-dispersive X-ray spectroscopy (EDS) mapping results (Supplementary Fig. 6) show that Cu and O elements are evenly distributed on the surface of h-Cu/Cu₂O MPs, with an atomic ratio of Cu to O approximately 2.5:1. Accordingly, the comparing Cu 2p spectra (Fig. 1d) clearly suggest that two peaks at about 933 and 952 eV can be observed, assigning to Cu⁺ or Cu⁰, respectively^{35,36}. The change of O 1s signal before and after electrochemical reduction shows that h-Cu/Cu₂O MPs have more O in chemisorbed state after activation (Supplementary Fig. 7). Moreover, the Cu LMM AES spectrum (Fig. 1e) further confirms the existence of Cu⁺ and Cu⁰^{37,38}. To analyze the phase transformation of bulk Cu₂O during electroreduction, we conducted an in-situ XPS study, the schematic diagram of the setup is shown in Supplementary Fig. 8. It can be seen from Fig. 1f that within the range of test potential (−0.1 to −0.4 V versus RHE), the signal of Cu⁰ gradually increases with the increase of potential, and the potential is increased to −1.5 V. The Cu⁰ and Cu⁺ signals in h-Cu/Cu₂O MPs samples obtained after 1200 s reduction are still coexisting. In situ Raman spectroscopy (Fig. 1g) further confirms the surface reconstruction from Cu₂O to Cu evidenced by the gradually weakening peak intensity at 218 and 625 cm^{−1} upon the increasing applied voltages^{39,40}.

To confirm the unsaturated coordination environment, the Cu K-edge X-ray absorption near-edge spectra (XANES) were carried out as exhibited in Fig. 2a. The pre-edge of the Cu K-edge absorption edge position for h-Cu/Cu₂O MPs NWs is close to Cu yet shift to lower energy compared to that of pure Cu₂O, which gives direct evidence for the partial surface reduction derived unsaturated coordination of the Cu⁰ in h-Cu/Cu₂O MPs²⁵. The Fourier transform extended X-ray absorption fine structure (FT-EXAFS) curves of h-Cu/Cu₂O MPs for Cu–O and Cu–Cu bond (Fig. 2b, c) increased from 1.84 to 1.86 Å and from 2.57 to 3.01 Å, respectively, compared with those of pure Cu₂O, suggesting the structural distortion of h-Cu/Cu₂O MPs due to the introduction of Cu⁰. The coordination structure of the h-Cu/Cu₂O MPs was further analyzed by fitting the k₃-weighted FT-EXAFS curves. As shown in Supplementary Table 4, the coordination number (CN) of the Cu–Cu in Cu₂O is about 6.6, which decreased to 5.4 in h-Cu/Cu₂O MPs, demonstrating that the Cu atom with unsaturated coordination environment was indeed generated after the electrochemical reduction treatment. The wavelet transform (WT) EXAFS analysis in both K and R spaces (Fig. 2d) provides intuitive indication for the difference in Cu–O and Cu–Cu coordination in h-Cu/Cu₂O MPs.

The urea electrosynthesis performance of h-Cu/Cu₂O MPs was measured in an H-type electrolytic cell (Supplementary Fig. 9). The concentration of NO₃[−] was set to 0.05 M, which was obtained through concentration treatments of nitrate wastewater, including evaporation and reverse osmosis. The comparing LSV curves (Fig. 3a) show that it exhibits the highest current density with the coexistence of NO₃[−] and CO₂ in the electrolyte, compared with that with only NO₃[−] or CO₂, implying the possible C–N coupling reaction. The amounts of urea and ammonia produced were then quantitatively determined by both diacetylmonoxime method and NMR (Methods and Supplementary Figs. 10–15). *I*–*t* tests were performed for 2 h for each potential in the range −0.2 to −0.6 V (versus RHE) in the flow-cell (Supplementary Fig. 16). According to the violet–visible (UV–Vis) results (Supplementary Fig. 17), the urea yield rate can reach as high as 632.1 ± 26.3 μg h^{−1} mg_{cat.}^{−1} under a superior FE of 43.2 ± 5.1 % for h-Cu/Cu₂O MPs at −0.3 V versus RHE (Fig. 3b). In addition, the FE of other major products including ammonia, carbon monoxide, nitrite, formic acid, C₂⁺ product and hydrogen was calibrated as shown in Fig. 3c.

We also studied the relationship between the HER (Hydrogen Evolution Reaction) and coupling reactions through the LSV curves of coupled reactions and HER (Supplementary Fig. 18). Meanwhile, Since there are more products in the nitrate reduction reaction at low potential, we independently studied the nitrate reduction performance of h-Cu/Cu₂O MPs, and found that the material has good nitrate reduction performance, and the nitrate reduction can produce ammonia and nitrite in the range of −0.2 to −0.6 V versus RHE, and can maintain about 80% of the total FE (Supplementary Fig. 19). This also provides a prerequisite for h-Cu/Cu₂O MPs to become a C–N coupled catalyst. Compared with metallic Cu and Cu₂O bulk, the h-Cu/Cu₂O MPs exhibits higher performance on urea yield rate and FE (Supplementary Fig. 20), which the synthetic of Cu in Supplementary Information. In addition, the product distribution of metallic Cu at various potentials, provided additional data in Supplementary Fig. 21. At the potential on −0.3 V (versus RHE), the Cu and Cu₂O have lower FE on coupling reaction (Cu: 0 % and Cu₂O: 5.32 ± 0.4%). To investigate the relationship between the interface and the electrochemical performance in urea synthesis, a series of comparative experiments were conducted. Firstly, the reduction of pure Cu₂O under our testing conditions (−0.3 V to −0.5 V versus RHE) resulted in the sample h-Cu/Cu₂O MPs, and the XRD curve comparison clearly shows that the reduction effect of Cu₂O under our testing conditions is not satisfactory (Supplementary Fig. 22). Secondly, a long-term stability test was performed on the h-Cu/Cu₂O MPs sample (Supplementary Figs. 23, 24). The change in material performance after 12 h of *i*–*t* testing showed good stability, confirming that the performance of h-Cu/Cu₂O MPs is minimally affected under our testing environment (neutral to slightly alkaline, potential −0.2 V to −0.6 V versus RHE).

To investigate the relationship between interface content and performance, two sets of comparative experiments were conducted, synthesizing two batches of samples: (1) Cu₂O bulk material was electrochemically reduced with a fixed reduction time of 1200 s, and the reduction potential was adjusted (0–1.8 V), resulting in a series of Cu/Cu₂O heterojunction samples (Supplementary Fig. 25). Urea electrochemical synthesis was performed under constant current for 2 h in a 0.05 M KNO₃ and CO₂ environment at −0.3 V vs. RHE. (2) Cu₂O bulk material was electrochemically reduced with a fixed reduction potential of −1.5 V vs. RHE, and the reduction time was adjusted (0–3600 s) to obtain a series of samples for performance studies (Supplementary Fig. 26). These samples were electrolyzed at −0.3 V vs. RHE for 2 h for the electrochemical synthesis of urea under the conditions of this study. The results showed that at the initial stage of increasing interface content, the electrochemical performance of urea was positively correlated with the interface content. When the interface content reached a certain level (synthesis conditions: −1.5 V vs. RHE, 1200 s), the electrochemical performance of urea tended to saturate. Previous extensive studies have shown that Cu₂O is completely reduced to pure Cu at high potentials. Therefore, we also investigated the performance when Cu₂O was completely reduced to pure Cu (Supplementary Fig. 20), and the results indicated a significant decrease in the electrochemical synthesis performance of urea on pure Cu. It can be concluded that as the reduction proceeds further, the degree of Cu₂O reduction to pure Cu increases, the interface content decreases, and the electrochemical performance for urea synthesis declines from its peak to a lower level comparable to pure Cu. In summary, the relationship between interface content and electrochemical urea synthesis initially shows a positive correlation, with the electrochemical performance reaching a peak and tending to saturate as the interface content reaches a certain level. When completely reduced to Cu, the interface disappears, and the urea performance significantly decreases.

Moreover, electrochemical active surface area (ECSA) was explored corresponding to the above samples (Supplementary Figs. 27, 28). The calculated *ecsa* is 93.5 cm², and the current density curves under different potentials are normalized (Supplementary

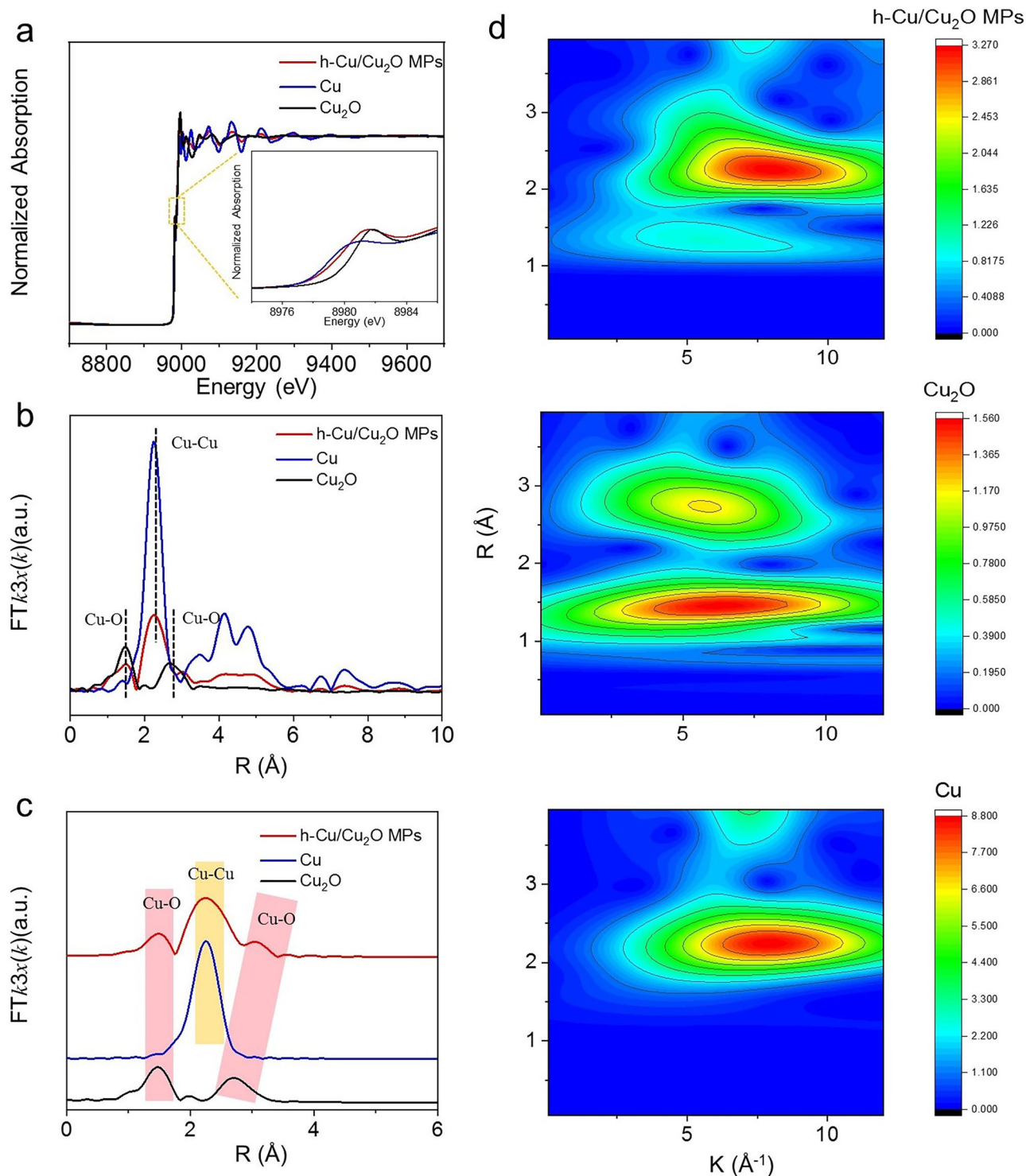


Fig. 2 | The coordination environment of Cu. **a** Cu K-edge XANES spectra and **(b)** the corresponding k₃-weighted $\chi(k)$ functions of the FT-EXAFS spectra for h-Cu/Cu₂O MPs, Cu₂O and Cu foil. **c** FT-EXAFS fitting curves for h-Cu/Cu₂O MPs, Cu₂O,

and Cu foil and **(d)** WT for the k₃-weighted EXAFS signals of h-Cu/Cu₂O MPs, Cu₂O and Cu foil. Source data for Fig. 2 are provided as a Source Data file.

Fig. 28). To demonstrate the practicability, we utilized a flow cell with gas diffusion layer (GDL) electrodes, featuring an h-Cu/Cu₂O MPs cathode paired with a nickel foam anode, separated by a Nafion membrane (Fig. 3d). Compared with the H-type cell, the flow cell can further promote the urea yield rate up to 883.6 $\mu\text{g h}^{-1}\text{mg}_{\text{cat}}^{-1}$ (Supplementary Fig. 29). The *i*-*t* test and CA result (Supplementary Fig. 30) exhibits the high stability of h-Cu/Cu₂O MPs, with a 20 mA cm⁻² current density decay after 12 h. In addition, the distribution diagram of

electrochemically synthesized products in the flow cell system in the range of -0.2 to -0.6 V versus RHE is shown in Supplementary Fig. 31. The error-bar versions of Fig. 3c and Supplementary Fig. 31 are represented in Supplementary Fig. 32. We compared our urea synthesis performance with published literature and found that despite using a much lower potential than the state-of-the-art catalysts reported in the literature, our catalyst achieved comparable urea yield rate and FE, indicating its high efficiency for urea synthesis and the

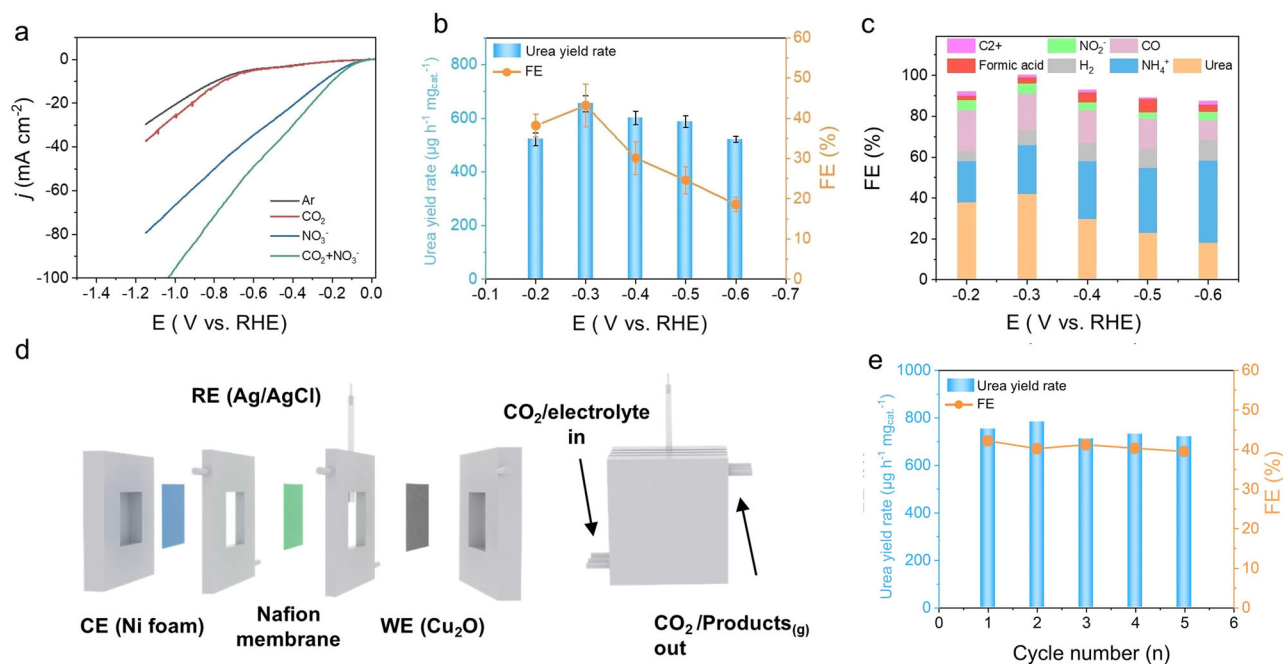


Fig. 3 | Electrochemical synthesis of urea from h-Cu/Cu₂O MPs. **a** LSV curves of h-Cu/Cu₂O MPs in Ar, CO₂, NO₃⁻, and NO₃⁻ + CO₂ saturated 0.5 M KHCO₃ electrolyte in the flow-cell. **b** Urea yield and Faraday efficiency of h-Cu/Cu₂O MPs at different applied potentials and **(c)** product distribution in the H-cell. **d** Schematic diagram

of three-electrode flow cell. **e** Consecutive urea synthesis stability test at -0.3 V versus RHE over h-Cu/Cu₂O MPs in three-electrode flow cell. Error bars show the standard deviations calculated from three independent experiments. Source data for Fig. 3 are provided as a Source Data file.

potential for energy savings. (Supplementary Table 1). Such high urea yield and FE can maintain outstanding stability with five successive runs (Fig. 3e) and CA results.

The relatively small current density has been considered as one of the limitations for scalable applications. In order to reduce the potential of urea synthesis process to increase urea yield, the lower thermodynamic potential of hydrazine oxidation (-0.33 V vs RHE) is utilized to replace the anodic OER reaction (Fig. 4a), which can effectively enhance the current density of two-electrode system (Fig. 4b). To investigate other reactions in the two-electrode system, such as the oxidation of urea at the anode and the reduction of hydrazine at the cathode, we conducted a study. Firstly, we examined the LSV curves with and without urea in the system (Supplementary Fig. 33). It is evident that the LSV curves, with and without urea, essentially overlap within the potential range of 0–1.8 V. Combining this with our study on the Faradaic efficiency of formic acid as a product (Supplementary Fig. 34), we conclude that under the conditions of this study, urea does not undergo oxidation at the anode within the potential range of 0 to -1.8 V. It is challenging to rule out trace reactions such as the reduction of hydrazine at the cathode; therefore, we also investigated the system with a membrane flow cell. By comparing the LSV and the variations in other product contents with and without the membrane, we can infer that some potential reactions in the membrane system do not significantly impact the final performance under our testing conditions (Supplementary Figs. 35, 36). To investigate the stability of the two-electrode system, both the cycling stability and long-time *i*-*t* test at 1.5 V are conducted (Fig. 4c, d). In addition, the FE change of the material during the 20 h *i*-*t* test is also detected at a unit interval of 5 h (Supplementary Fig. 37), which clearly suggest the durability. Inspiringly, the N_{urea}-selectivity can reach as high as 80 ± 3.6% at -0.4 V versus RHE (Fig. 4e). The N¹⁵ isotopic labeling method (Fig. 4f and Supplementary Fig. 38) is utilized to confirm the source of the urea product^{8,10}. Furthermore, the reliability of the results is also validated by measuring the yield rate within both UV and nuclear magnetism method (Fig. 4g), where good agreement can be observed.

In order to explore the specific component information of the intermediates, we conducted a series of in-situ electrochemical experiments, including advanced in situ Raman experiments and operando SR-FTIR measurements (Supplementary Figs. 39–41), which are highly sensitive to the generated intermediates⁴¹. The in-situ Raman data in Fig. 5a were obtained in a three-electrode system under conditions of -0.1 to -0.4 V versus RHE, with electrochemical reduction performed for 5 min at each potential. The signal changes indicate a significant increase in the C–N signal at 1000 cm⁻¹ with the increase of potential, providing strong evidence for the occurrence of C–N coupling⁴². Furthermore, with the increase of potential, the signals of NO₃⁻ at 1062 cm⁻¹ and HCO₃⁻ at 1396 cm⁻¹ in the electrolyte system significantly decreased. In situ Raman experiments revealed the content changes of C and N species during the C–N coupling reaction.

To further investigate the information of intermediates during the reaction process, in situ infrared experiments were conducted. The infrared signals were collected from 1100 to 3500 cm⁻¹ during the negative scan from -0.1 to -0.7 V versus RHE, with electrochemical reduction performed for 5 min at each potential. As shown in Fig. 5a, it can be clearly observed that the C–N bond formation was favorably demonstrated, and the rate of C–N bond formation gradually increased when tested at -0.3 V in the range of 1100 to 1800 cm⁻¹^{43,44}. Operando SR-FTIR results from 2800 to 3500 cm⁻¹ confirmed the emergence of the N–H bending mode at 2940 cm⁻¹, which started to appear from -0.3 V (Fig. 5b). In the range from 1100 to 1800 cm⁻¹, infrared bands were probed at 1737 cm⁻¹ (Fig. 5c), which are assignable to the bending mode and rocking mode of C=O in urea. Infrared bands were probed at 1280 and 1144 cm⁻¹, which originate from the bending and rocking modes of the -NH₂ bond in urea¹¹. In addition to the infrared bands of C=O and -NH₂, the stretching mode of C–N can be observed at 1450 cm⁻¹⁹. Evidenced by the operando SR-FTIR results, the C–N coupling is successfully realized for subsequent urea synthesis, correlating well with the electrocatalysis experiments. In contrast with free urea, the stretching frequency shift of C–N implies that urea

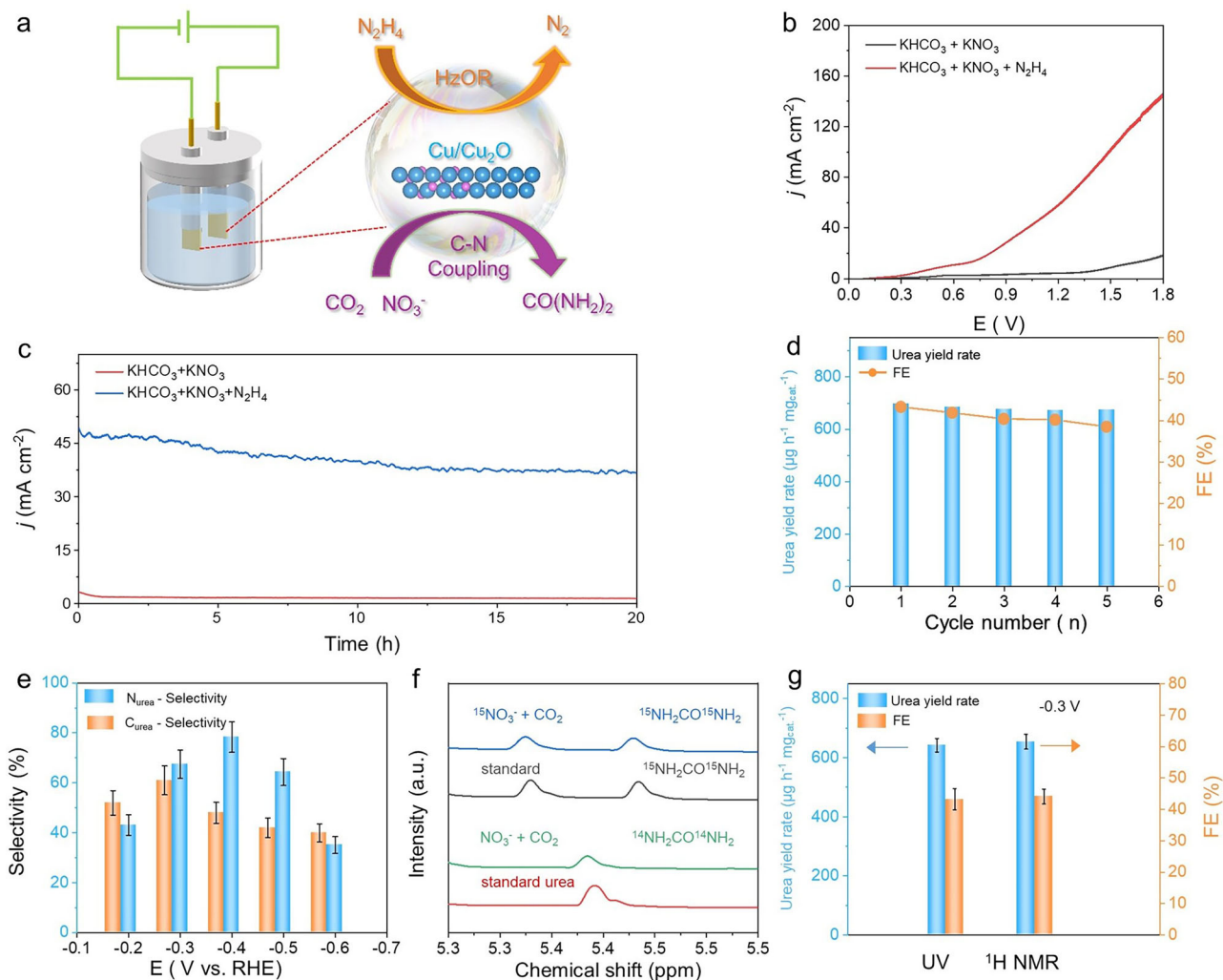


Fig. 4 | Electrochemical synthesis of urea coupled with hydrazine Hydrate Oxidation Reaction in a two-electrode system. a Schematic diagram of Two electrode cell. **b** LSV curves in different electrolytes. **c** Chrono-amperometry curves in different electrolytes for 20 h. **d** Consecutive urea synthesis stability test over h-Cu/Cu₂O MPs of two-electrode flow cell at 1.5 V. **e** Selectivity at different applied

potentials of three-electrode flow cell. **f** ¹⁵N isotope labeling test of three-electrode flow cell at -0.3 V versus RHE. **g** Comparison of UV and ¹H NMR test results. Error bars show the standard deviations calculated from three independent experiments. Source data for Fig. 4 are provided as a Source Data file.

has coordinated with the existence of surface heterointerfaces (Cu/Cu₂O) through the oxygen atom of the C=O group.

Additionally, the NHCO vibrational band arises at 1698 cm⁻¹ (Fig. 5d)⁴⁵. With the change of chemical bond energy under the accumulation of binding potentials, we can conclude that the strengthening of NHCO and C-N is synchronous, while the C=O bond gradually weakens with the formation of C-N. In summary, in-situ infrared Raman and infrared experiments confirm that h-Cu/Cu₂O MPs, as a catalyst, indeed form C-N chemical bonds in the electrolyte environment.

Density functional theory (DFT) calculations were performed to investigate the source of site activity and the mechanism of C-N coupling on the Cu/Cu₂O interface. Accurate models are needed to describe the Cu atom (Cuⁱ) at the interface. Cuⁱ is the active site for C-N coupling and should have an O coordination number between Cu⁰ (pure Cu atom), Cu^{cus} (low-coordinated Cu₂O atom), and Cu^{csa} (the coordinatively saturated copper)^{46–48}. The h-Cu/Cu₂O MPs model is shown in Fig. 6a, and the Cu₂O and Cu models are presented in Supplementary Figs. 42, 43, respectively (see SI section for modeling methods). The Cu₂O (111) surface on the left and the Cu (111) surface on the right form a stable interface, and the Cu site in the middle is sufficient to accurately describe Cuⁱ. Due to the breaking of O

coordination, Cuⁱ has a unique electronic structural characteristic, as demonstrated by the results of the Bader charge (Fig. 6b). On the surface of the site, Cuⁱ lost an average of 0.2 e, Cu⁰ lost an average of 0 e, Cu^{csa} lost an average of 0.5 e, and Cu^{cus} lost an average of 0.3 eV. Meanwhile, the differential charge between the Cu₂O (111) phase and the Cu (111) phase (Fig. 6c) confirms that there is a built-in electric field between the two phases, and the electrons of the Cu (111) on the right tend to flow to the Cu₂O (111) on the left, which is consistent with the conclusion of Fig. 6b⁴⁹.

To facilitate understanding, the occurrence of C-N coupling usually requires two significant conditions. Firstly, there must be a suitable competitive reaction relationship, meaning that the energy barrier of a C-N coupling reaction is lower than that of any competitive reaction, such as the hydrogenation and desorption of N and C intermediates⁵⁰. Secondly, the two active sites for trapping the C and N intermediates should be adjacent, and there should be no strong steric effects^{18,51}. To explain the source of Cuⁱ C-N coupling activity, we calculated the free energy of the entire reaction path step by step. For each elementary reaction, we considered the competitive relationships of hydrogenation, adsorption, desorption, and coupling reactions, and the easiest direction of each step would determine the intermediate energy to be considered in the next step. Based on this,

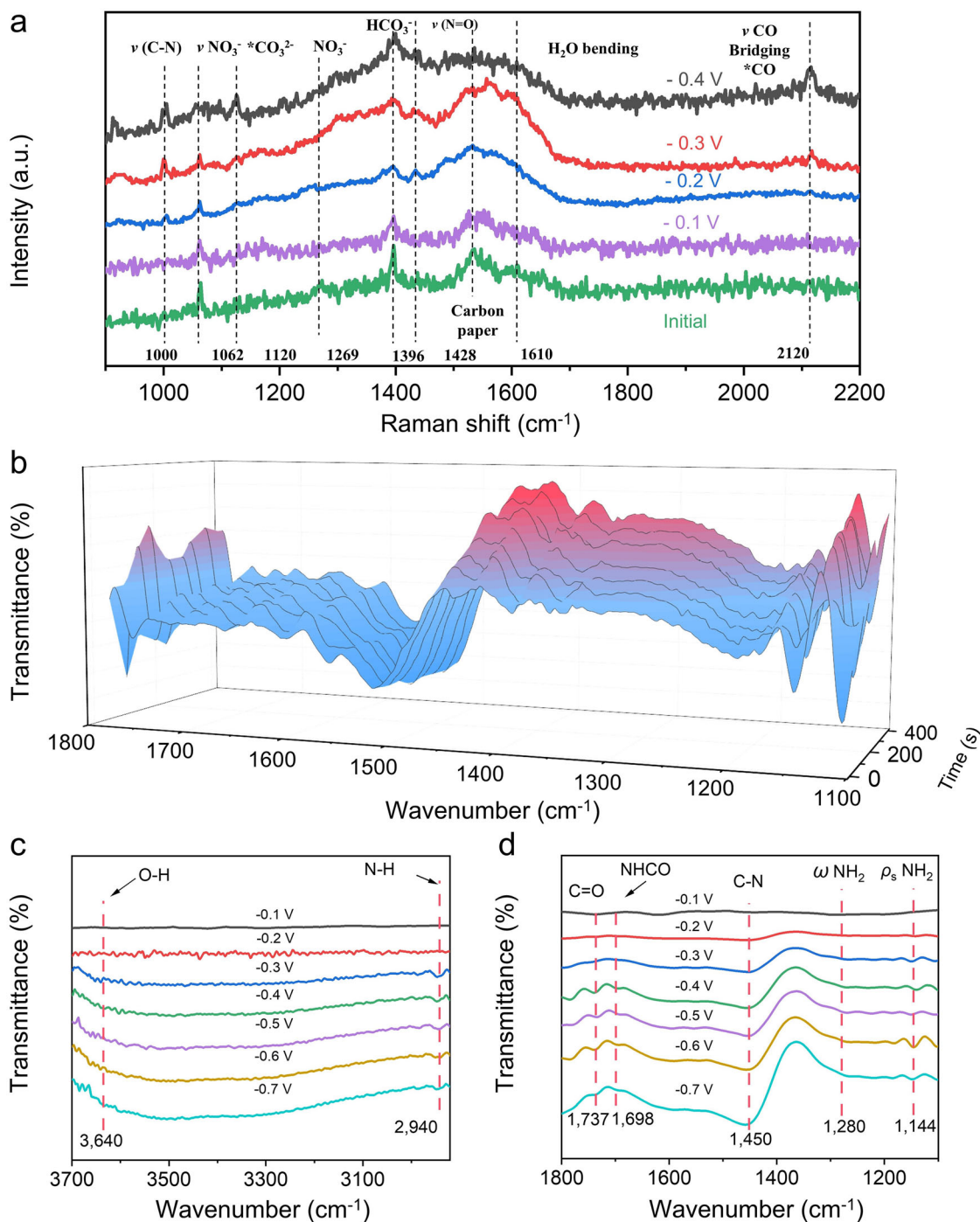


Fig. 5 | In situ electrochemical Raman and Operando Synchrotron radiation Fourier Transform Infrared Spectroscopy (FTIR) measurements under various potentials for h-Cu/Cu₂O MPs during Electrochemical synthesis of urea. a In situ Raman diagram under electrochemical C–N coupling test conditions.

b Infrared signals in the range of 1100–1800 cm^{-1} at different times (0–400 s). **c** Infrared signals in the range of 2920–3700 cm^{-1} and in the range of **(d)** 1100–1800 cm^{-1} under various potentials for h-Cu/Cu₂O MPs during the electro-coupling of NO_3^- and CO_2 . Source data for Fig. 5 are provided as a Source Data file.

we investigated the possibility of C–N coupling at the Cu^{I} site of h-Cu/Cu₂O MPs, the Cu^0 site of Cu (111), and the Cu^{CUS} site of Cu₂O (111). For the Cu (111) surface, the energy barrier of the hydrogenation reaction of N intermediates is always lower than that of C–N and CO_2 . Fast NO_3RR causes Cu (111) to fail to form C–N bonds. Meanwhile, it has been demonstrated that Cu^{CUS} on the Cu₂O (111) surface have high CO_2RR and NO_3RR performance, which provides an opportunity for C–N coupling. However, the results show that for two adjacent Cu^{CUS} sites, the adsorption of N intermediates at one site will inhibit the activation of CO_2 by the adjacent Cu^{CUS} . This may be due to the steric

effect of neighboring Cu^{CUS} in the form of $\text{Cu}^{\text{CUS}}\text{--Cu}^{\text{CSA}}\text{--Cu}^{\text{CUS}}$ distribution, which introduces stronger repulsion of C intermediates and N intermediates. Moreover, it is difficult for CO_2 with stable $\text{C}=\text{O}$ to form C–N bonds with N intermediates, resulting in the dominant hydrogenation reaction of N intermediates at Cu^{CUS} sites. Therefore, C–N coupling is unlikely to occur in Cu₂O (111).

Surprisingly, the adsorption of N intermediates at the Cu^{I} site of h-Cu/Cu₂O MPs promotes the activation of adjacent Cu^{I} sites towards CO_2 . In addition, we conducted a series of density functional theory (DFT) calculations (Supplementary Figs. 44, 45). These results indicate

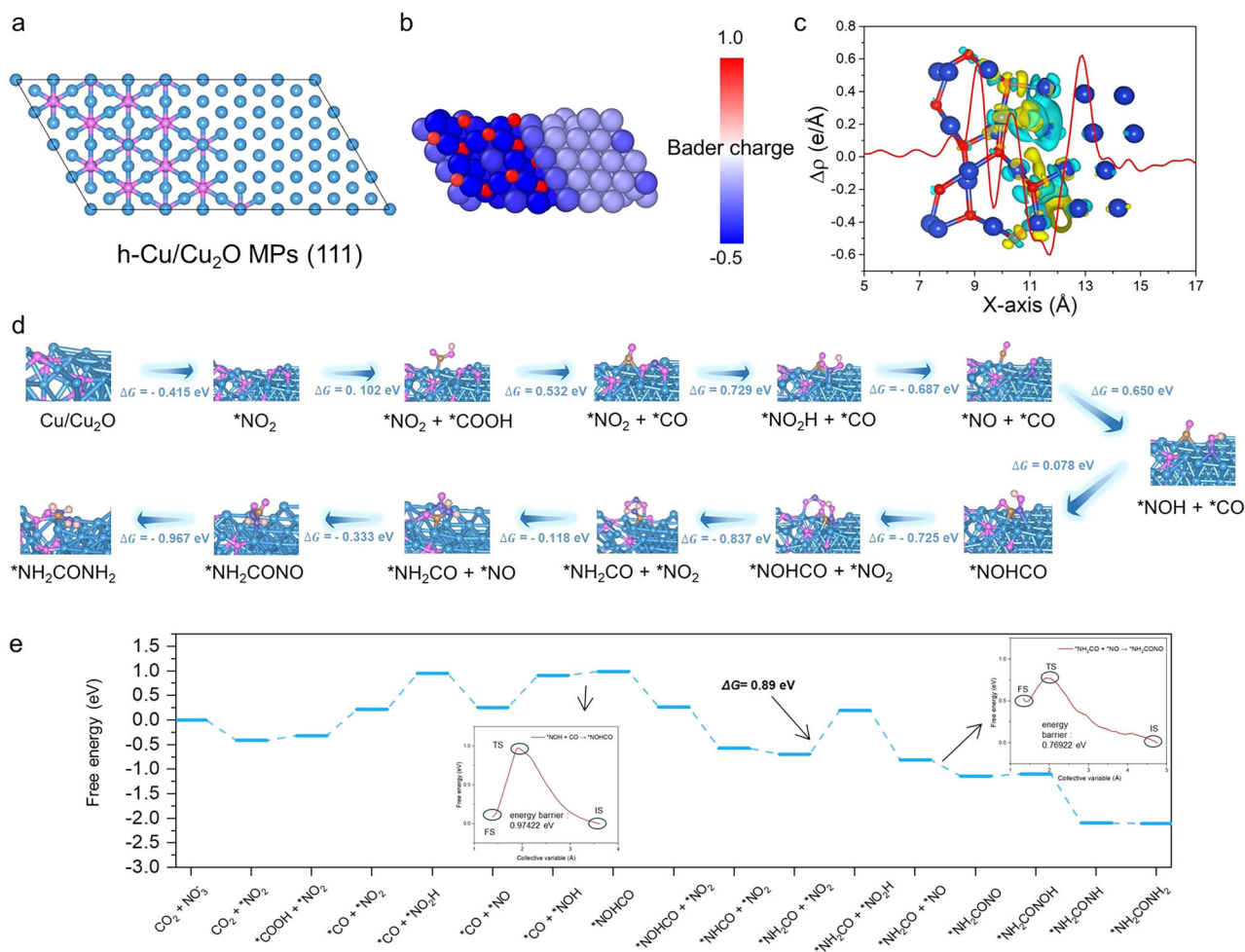


Fig. 6 | DFT calculations. **a** DFT-optimized structures of h-Cu/Cu₂O MPs. **b**, **c** Bader Charge and Charge density difference for the h-Cu/Cu₂O MPs. The red and blue colors indicate charge accumulation and depletion, respectively. **d** Reaction pathways, schematic diagrams of intermediate adsorption configuration and

corresponding energy changes of urea electrosynthesis for h-Cu/Cu₂O MPs. **e** Free energy diagram of urea electrosynthesis on h-Cu/Cu₂O MPs. Source data for Fig. 6 are provided as a Source Data file.

that the presence of NO₂ at the Cu/Cu₂O interface is conducive to the protonation of CO₂, but this phenomenon does not exist at the simple Cu and Cu₂O sites. The energy barrier of CO₂ hydrogenation activation decreases from 0.75 to 0.11 eV after the formation of NO₂, which is attributed to the unique electronic structure of the Cuⁱ site induced by O coordination breaking. This structure enables the Cuⁱ site to adsorb N intermediates and greatly promote the activation of adjacent Cuⁱ sites towards CO₂. As a result, the C–N coupling of N intermediates adsorbed at Cuⁱ sites does not rely on CO and CO₂ from solution, but rather on local sampling of CO from nearby Cuⁱ sites. Unlike Cu^{CUS}, naturally occurring Cuⁱ does not have a steric effect and has a suitable competitive relationship to promote the occurrence of C–N coupling. The step-by-step calculation details are shown in Supplementary Figs. 46–50. Previous studies have also reported that N intermediates can enhance CO₂ activation⁶. To investigate this phenomenon, we employed stepwise calculations to construct various implicit solvent adsorption models at the Cu, Cu₂O, and Cu/Cu₂O interfaces. The C–N coupling pathway obtained at the h-Cu/Cu₂O MPs interface is shown in Fig. 6d. The first step of C–N coupling occurs at CO–NOH, with an energy barrier of 0.078 eV, lower than the hydrogenation reactions of NOH and CO (0.89 eV and 1.49 eV, respectively). At the same time, the transition state energy of this process is calculated, and the calculated energy barrier is 0.97422 eV (Fig. 6e, Supplementary Fig. 51), which is compared with the published results (Supplementary Table 2). The final rate-determining step of the entire reaction occurs at the

hydrogenation of NO₂, with an energy barrier of 0.89 eV, which is compared with the published results (Supplementary Table 3). The solvation effect is the key to obtain more accurate electrocatalytic simulation results, and the above calculation processes are obtained under the solvation model. Overall, these findings shed light on the mechanism underlying the high C–N coupling performance of Cuⁱ and provide insights into the design of efficient catalysts for CO₂ conversion.

The protonation of CO₂ demands an energy input of 0.75 eV, unlike the spontaneous formation of *NO. This results in a high accumulation of *NOH on the catalyst surface during electrocatalysis, obstructing CO₂ adsorption and reduction of h-Cu/Cu₂O MPs. A localized h-Cu/Cu₂O MPs configuration supports electron transfer to *CO₂, enabling C–N bond formation through the reaction of these intermediates. The energy barrier for *CONOH formation is significantly lower (0.078 eV) compared to the 0.729 eV required for protonating *NO₂ to *HNO₂, favoring early-stage C–N coupling (Fig. 6e). These findings highlight the critical role of the (111) crystal planes in promoting selective urea synthesis⁸. Referring to the electrocatalysis results, the lower energy increase for C–N coupling and the spontaneous formation of *NO₂ might synergistically determine the extremely high values of Curea-selectivity and Nurea-selectivity. The subsequent reduction steps are exothermic, and the urea can be easily desorbed from the h-Cu/Cu₂O MPs surfaces. A detailed reaction mechanism with the most stable geometric structures of the reactants, intermediates

and products throughout the urea formation is listed in the computational method. Similarly, the model and reaction steps of pure Cu and Cu₂O were calculated which shown in Supplementary Figs. 52–59. The computational results reveal that the presence of exist of C–N coupling reaction and the corresponding mechanistic of urea synthesis.

In conclusion, we have successfully constructed h-Cu/Cu₂O MPs catalysts through a straightforward electroreduction process, and demonstrated their effectiveness in the co-reduction of CO₂ and NO₃[−] pollutants for the production of urea. High-resolution characterization techniques, such as XANES, confirmed the presence of the interface and unsaturated coordination of Cu. We also found that the optimized faradaic efficiency and yield for urea on h-Cu/Cu₂O MPs were significantly higher than those on Cu and Cu₂O alone. Through a combination of in situ ATR-FTIR and DFT analysis, we established that the electron transfer from the Cu₂O shell to the Cu facilitates the formation and coupling of *CO and *NOH intermediates, leading to enhanced catalytic performance. Overall, this work presents a rational approach for the fabrication of efficient catalysts towards the sustainable production of carbon-nitrogen chemicals from CO₂ and nitrate under ambient conditions.

Methods

Materials

Carbon papers (HCP020N, thickness: 0.19 ± 0.01 mm) were obtained from Hesen Company (Shanghai, China). Methanol (CH₃OH), isopropanol (C₃H₈O), *N,N*-dimethylformamide (DMF), hydrogen peroxide (H₂O₂, 30% aqueous solution), ammonium chloride (NH₄Cl), potassium chloride (KCl, AR), potassium hydroxide (KOH, AR), and sodium hydroxide (NaOH, AR) were purchased from Sinopharm Chemical Reagent Co., Ltd. KHCO₃ (≥99.99% metals basis, 99.7–100.5% dry basis), copper (I) oxide (Cu₂O), and isotopically enriched K¹⁵NO₃ (99 atom% isotopic abundance) were supplied by Aladdin Biochemical Technology Co., Ltd. Sodium nitroprusside dihydrate (Na₂[Fe(CN)₅NO]·2H₂O) was sourced from Energy Chemical. Sodium hypochlorite (NaClO, 11–15% available chlorine) was procured from Thermo Scientific. Potassium nitrate (KNO₃, >99%) came from Sinopharm Chemical Reagent Co., Ltd. Gases including CO₂ (99.99%) and Ar (99.999%) were purchased from Airgas. All reagents were utilized as supplied without further purification unless otherwise indicated.

Synthesis of catalysts

Synthesis of metallic Cu. The metallic Cu electrode were synthesized via a facile one-step electroreduction process. In a typical procedure, using commercial Cu₂O powder as working electrode. The commercial were in situ electrochemical reduced at −2.05 V (vs. RHE) for 12 h in an Ar-saturated 0.5 M KHCO₃ solution. The final product is denoted as Cu.

Synthesis of h-Cu/Cu₂O MPs

The Cu/Cu₂O electrode were synthesized via a facile one-step electroreduction process. In a typical procedure, using commercial Cu₂O powder as working electrode. The commercial were in situ electrochemical reduced at −1.5 V (vs. RHE) for 1200 s in an Ar-saturated 0.5 M KHCO₃ solution. The final product is denoted as Cu/Cu₂O.

Materials characterization

The morphology and structure of the samples were analyzed using various characterization techniques. Field-emission scanning electron microscopy (FESEM, JSM-6700F) and transmission electron microscopy (TEM, JEOL, JEM-2010) were employed to observe the surface and internal structures. Powder X-ray diffraction (XRD, TTR-III) and Raman spectroscopy (LabRamHR) with a 532 nm laser were utilized to study the crystalline phases and vibrational properties. High-resolution TEM (HRTEM) and energy dispersive spectroscopy (EDS) mapping were performed on a Talox F200X transmission electron microscope (Thermo Fisher Scientific, USA) operating at 200 kV. The

chemical states of the samples were analyzed using an ESCALAB 250 X-ray photoelectron spectrometer equipped with an Al K α X-ray source ($h\nu$ = 1486.6 eV). Elemental compositions were determined using a PerkinElmer Optima 7300 DV ICP atomic emission spectrometer. Proton nuclear magnetic resonance (¹H NMR) spectra were recorded on an Avance II 400 spectrometer (Bruker). Gas chromatography (GC 7900) with a TDX-01 column and thermal conductivity detector was used to analyze generated gases, which were sampled with a SCE syringe. Potential-dependent Raman spectroscopy was conducted under controlled applied potentials in 0.5 M KHCO₃ with CO₂ bubbling. The electrocatalyst was stabilized for 300 s at the desired potential to ensure steady-state conditions before recording each spectrum.

Electrochemical measurements

The electrolyte consisted of a mixed solution of 0.5 M KHCO₃ and 0.05 M KNO₃ (conductivity: 18.25 M Ω cm^{−1}). During the test, equal volumes of electrolyte (40 mL each) were added into the cathodic and anodic chambers of the electrolytic cell. The electrolyte was purged sequentially with high-purity Ar and CO₂ for 10 min each before the test. The prepared electrolyte requires no additional storage conditions other than room temperature⁸.

Before the electrocatalytic C–N coupling test, CO₂ gas was continuously supplied into the cathodic chamber at a flow rate of 30 mL min^{−1}, with the cathodic electrolyte consisting of a mixed solution of 0.05 M KNO₃ and 0.5 M KHCO₃. In isotope labeling experiments, the nitrogen source was replaced with K¹⁵NO₃. Electrocatalytic experiments were conducted in H-type and flow cells with a three-electrode configuration, using a CHI760E electrochemical workstation (CH Instruments Inc., China). The reference electrode was an Ag/AgCl electrode filled with saturated KCl solution, and the counter electrode was a carbon rod. In this study, all potentials were referenced to the Ag/AgCl electrode and converted to the RHE scale using the formula: ERHE = EAg/AgCl + 0.0591 × pH + 0.197 V, where pH is the average pH of the electrolyte. The pH of the electrolyte was measured with a pH meter (Mettler Toledo), with the pH of CO₂-saturated electrolyte being 6.8 ± 0.03, and that of Ar-saturated electrolyte being 8.3 ± 0.06. The *I*–*t* curves were obtained by setting the applied potential (versus RHE) and electrolysis time using chronoamperometric measurements. The LSV curves were recorded by linear sweep voltammetry with a negative scan mode over a potential range from 0.0 V to −2.0 V (versus RHE).

The cathodic and anodic chambers were separated by a Nafion 117 membrane (geometric area: 2 × 2 cm², thickness: 183 μ m). The pretreatment process for the Nafion membrane was as follows: The Nafion 117 membrane was immersed in a 5% H₂O₂ aqueous solution and boiled at 80 °C for 1 h to remove organic impurities. Then, the membrane was repeatedly rinsed with deionized water and immersed in deionized water at 80 °C for 1 h to completely remove any residual H₂O₂. The Nafion membrane was stored in deionized water at room temperature prior to use.

Electrocatalytic experiments were conducted in both H-type and flow cells with a three-electrode configuration, using a CHI760E electrochemical workstation (CH Instruments Inc., China). The *I*–*t* curves were recorded by applying a set potential (versus RHE) and electrolysis time, using a chronoamperometric method. The LSV curves were obtained via linear sweep voltammetry with a negative scan mode over the potential range from 0.0 V to −2.0 V (versus RHE). The LSV and CV curves were recorded at a scan rate of 10 mV s^{−1}⁵².

For the chronoamperometry tests, the working electrode was prepared by modifying carbon paper with a catalyst. Initially, the carbon paper was annealed at 400 °C for 16 h to enhance its hydrophilicity. After cooling, the paper was cut into rectangular pieces with a geometric area of 1 × 1 cm². A catalyst ink was prepared by dispersing 5 mg of catalyst and 20 μ L of Nafion solution (5 wt%) into 480 μ L of a dispersant mixture (isopropyl alcohol: water = 2:1) and sonicated for

40 min to form a uniform mixture. The catalyst ink (100 μL) was then drop-cast onto the carbon substrate and allowed to dry naturally, resulting in a catalyst loading of 1 mg cm^{-2} .

In situ Raman spectroscopy

In-situ Raman spectroscopy was carried out using a Renishaw inVia Confocal Raman Microscope, equipped with a 50X (0.5 N.A.) long working distance objective (Olympus). A 532 nm excitation laser with a power of 2.5 mW and an 1800 lines/mm diffraction grating was used for the measurements. The working electrode, made of carbon paper (1.5 cm \times 1.5 cm), was paired with a titanium wire as the counter electrode and an Ag/AgCl (saturated KCl) as the reference electrode. Raman spectra were recorded under applied potentials in a 0.5 M K_2SO_4 electrolyte, with the electrocatalyst held at the specified potential for 300 sec to achieve steady-state conditions before each measurement. For each spectrum, 15 sweeps were collected within the range of 175 to 1900 cm^{-1} .

In situ XPS measurements

In situ XPS measurements were conducted using an ambient pressure XPS setup integrated with a static electrochemical cell. The counter electrode was a platinum (Pt) wire, while the reference electrode consisted of a Pt wire coated with Ag/AgCl paste. The working electrode was carbon paper, loaded with a Cu_2O bulk catalyst, shaped into a 5.5 mm diameter circle. During the in-situ XPS analysis, both the counter and reference electrodes were submerged in the electrolyte and sealed with a Nafion membrane. The carbon paper electrode was placed between the Nafion membrane and a tantalum (Ta) foil to ensure proper electrical connection. The analysis chamber was maintained at a pressure of approximately 0.3 mbar. For the i - t mode electrochemical tests, the applied potential range was set between -0.1 V and -0.4 V vs. RHE, with each potential held for 1 h.

Operando SR-FTIR measurements

Operando SR-FTIR measurements were performed at the BL01B infrared beamline of the National Synchrotron Radiation Laboratory (NSRL) in China, using a custom-designed top-plate cell-reflection infrared setup with a ZnSe crystal as the infrared transmission window, with a cutoff energy of approximately 625 cm^{-1} . The setup was equipped with an FTIR spectrometer (Bruker 70 v/s), a KBr beam splitter, and a liquid nitrogen-cooled mercury cadmium telluride (MCT) detector. An infrared microscope (Bruker Hyperion 2000) with a $\times 15$ objective was used. The electrochemical setup and cell configuration are shown in Supplementary Fig. 38. To ensure high-quality SR-FTIR spectra, the system operated in reflection mode, and each infrared absorption spectrum was acquired by averaging 128 scans with a resolution of 4 cm^{-1} . The background spectrum of the catalyst electrode was recorded at open-circuit voltage before each measurement, and the measured potential ranges for the electrocatalytic reaction were from -0.1 to -0.7 V (vs. RHE) with a potential step of 0.1 V.

Determination of urea

The urea in the cathodic electrolyte was determined spectrophotometrically using the diacetylmonoxime method. The color development procedure was as follows: 1 mL of the electrolyte was taken, and 1 mL of DAMO-thiosemicarbazide (TSC) solution (5 g DAMO and 100 mg TSC dissolved in 1000 mL of deionized water) and 2 mL of acid-ferric solution (100 mL concentrated phosphoric acid, 300 mL concentrated sulfuric acid, 600 mL deionized water, and 100 mg ferric chloride) were added. The solution was mixed thoroughly and then heated to 100 $^{\circ}\text{C}$ for 20 min. After cooling to room temperature, the absorbance was measured using a UV-Vis spectrophotometer (Shimadzu UV-2700) at 525 nm, as shown in Supplementary Figs. 9, 10, where the urea absorption peak is observed.

Determination of ammonia

The determination of $\text{NH}_3\text{-N}$ was performed using Nessler's reagent as the colorimetric reagent. The procedure is as follows: a certain volume of cathodic electrolyte was diluted to 5 mL, followed by the addition of 0.1 mL of potassium sodium tartrate solution ($\rho = 500$ g/L) and 0.1 mL of Nessler's reagent. The solution was mixed thoroughly and allowed to stand for 20 min. The absorbance was measured at a wavelength of 420 nm. The concentration-absorbance curve was calibrated using a series of standard ammonium chloride solutions, with ammonium chloride crystals pre-dried at 105 $^{\circ}\text{C}$ for 2 h. Standard ammonia sulfate solutions were also used for calibration, as shown in Supplementary Figs. 11, 12, which contained the same electrolyte concentrations as those used in the electrocatalysis experiments.

Determination of hydrazine (N_2H_4)

The hydrazine presented in the electrolyte was estimated by the method of Watt and Chrisp⁸. The color reagent was prepared by mixing para-(dimethylamino) benzaldehyde (5.99 g), concentrated hydrochloric acid (30 mL), and ethanol (300 mL). To establish the calibration curve, a series of reference solutions were first prepared by pipetting appropriate volumes of hydrazine hydrate-nitrogen 0.1 M HCl solution into colorimetric tubes. The volume of each solution was then adjusted to 5 mL with diluted 0.1 M Na_2SO_4 electrolyte. Next, 5 mL of the prepared color reagent was added to each tube, and the mixture was stirred for 10 min at room temperature. The absorbance of the resulting solution was measured at 457 nm. Hydrazine yields were then calculated from the standard curve using 5 mL of residual electrolyte and 5 mL of the color reagent. Absolute calibration of the method was performed using known concentrations of hydrazine monohydrate solutions as standards, and the resulting calibration curve showed a strong linear correlation between absorbance and $\text{N}_2\text{H}_4\cdot\text{H}_2\text{O}$ concentration, based on three independent calibrations.

Determination of nitrite ions (NO_2^-)

The nitrite concentration was determined using UV-Vis spectroscopy with the following color reagent preparation: 0.02 g of N-(1-Naphthyl) ethylenediamine dihydrochloride and 0.4 g of p-aminobenzenesulfonamide were sequentially added to a mixture of 5 mL deionized water and 1 mL phosphoric acid, and the solution was thoroughly mixed. For the nitrite concentration measurement, a certain amount of catholyte was taken and diluted to 5 mL. Then, 0.1 mL of the prepared color reagent was added to the 5 mL solution and mixed thoroughly. After allowing the mixture to sit for 20 min, the absorbance was measured at 540 nm. A concentration-absorbance calibration curve was constructed using a series of standard NaNO_2 solutions.

Determination of carbon monoxide (CO), hydrogen (H_2) and dinitrogen (N_2)

The amounts of CO, H_2 , and N_2 were quantified by in-line gas chromatograph (7890B, Agilent) equipped with a TCD and an FID⁸.

Calculations of average urea yield rate and FE

The urea yield was determined by measuring the absorbance of the catholyte using a UV-Vis spectrophotometer. The urea concentration in the electrolyte was obtained by referencing a urea concentration-absorbance calibration curve. The yield was then calculated based on the test time, as shown in the following formula:

$$R_{\text{urea}} = (C^{\text{urea}} \times V) / (t \times m) \quad (1)$$

where c urea is the measured urea concentration ($\mu\text{g mL}^{-1}$), V is the total volume of electrolyte (mL), t is time (h) for electrocatalysis and m is the catalyst loadings (mg). The Faradaic efficiency (FE) for urea is the ratio of the charge consumed for urea synthesis during the electrolysis time to the total charge passed. It can be calculated using the following

formula:

$$FE = (16F \times C_{\text{urea}} \times V) / (60.06 \times Q) \quad (2)$$

where F is the Faraday constant ($96,485.3 \text{ C mol}^{-1}$) and Q is the total charge passed through the working electrode (C).

Calculations of average ammonia yield rate and FE

The ammonia yield rate is calculated by measuring the absorbance of the catholyte using a UV-Vis spectrophotometer, determining the ammonia concentration in the electrolyte based on a concentration-absorbance standard curve, and then using the testing time to calculate the yield. The specific formula is as follows:

$$R_{\text{NH}_3} = (C_{\text{NH}_3} \times V) / (t \times m) \quad (3)$$

where C_{NH_3} is the measured NH_3 concentration ($\mu\text{g ml}^{-1}$), V is the total volume of electrolyte (ml), t is time (h) for NO_3^- reduction reaction and m is the catalyst loadings (mg). The Faradaic efficiency (FE) for ammonia synthesis refers to the ratio of the charge used to produce ammonia during the electrolysis time to the total charge passed, and is calculated using the following formula:

$$FE = (8F \times C_{\text{NH}_3} \times V) / (17 \times Q) \quad (4)$$

where F is the Faraday constant ($96,485.3 \text{ C mol}^{-1}$) and Q is the total charge passed through the working electrode (C).

CER product analysis

The products obtained were analyzed using gas chromatography (GC) and ^1H NMR spectroscopy on a 400 MHz NMR instrument. Gaseous products from CO_2 reduction, such as carbon monoxide, methane, ethylene, ethane, and propylene, were detected and quantified using GC with a flame ionization detector (FID) and a nickel conversion furnace. Hydrogen was measured quantitatively with a thermal conductivity detector (TCD). The liquid products, including formic acid, were quantified using NMR, with dimethyl sulfoxide (DMSO) serving as the internal standard. For NMR analysis, 0.5 mL of KOH electrolyte, collected after electrolysis, was mixed with 100 μL of D_2O and 67 μL of DMSO containing 5 mM as the internal standard. The ^1H NMR spectra were recorded with water suppression using a pre-saturation technique. The Faradaic efficiency was determined based on a calibration curve using the following formula:

$$N_{\text{products}} = C_{\text{products}} \times V \times \text{NA} \times ne \quad (5)$$

$$N_{\text{total}} = Q/e \quad (6)$$

$$FE = N_{\text{products}} / N_{\text{total}} \times 100\% \quad (7)$$

where N_{products} is the total number of product transfer electron, C_{products} is the concentration of product, V is the volume of electrolyte or gases, NA: avogadro constant, $6.022 \times 10^{23} \text{ mol}^{-1}$, n is the number of electron transferred for product formation, e is the electron, Q is the number of transfer charge, N_{total} is the total number of transfer electron.

Calculations of N_{urea} -selectivity and C_{urea} -selectivity

The selectivity for urea production (N_{urea} -selectivity) was determined using the following equation:

$$N_{\text{urea}} - \text{selectivity} = n_{\text{urea}}(N) / n_{\text{total}}(N) \quad (8)$$

In this equation, $n_{\text{urea}}(N)$ refers to the number of moles of nitrogen present in the produced urea, while $n_{\text{total}}(N)$ represents the total moles of nitrogen in all the products obtained from nitrate⁸. The C_{urea} -selectivity was calculated as follows:

$$C_{\text{urea}} - \text{selectivity} = n_{\text{urea}}(C) / n_{\text{total}}(C) \quad (9)$$

Here, $n_{\text{urea}}(C)$ represents the number of moles of carbon found in the produced urea, and $n_{\text{total}}(C)$ refers to the total moles of carbon in all products derived from CO_2 ⁸.

Computational method

All calculations were conducted using the Vienna Ab Initio Simulation Package (VASP) with density functional theory (DFT). Projector augmented wave (PAW) pseudopotentials and the Perdew-Burke-Ernzerhof (PBE) exchange-correlation functional within the generalized gradient approximation (GGA) were applied. To capture long-range van der Waals (vdW) interactions, the DFT-D3 correction was used. A plane wave energy cutoff of 500 eV was employed, and the self-consistent field (SCF) convergence criterion was set to 10^{-5} eV. Geometry optimization was performed using the conjugate gradient method, with forces on each atom converging below 0.03 eV/\AA^3 . The implicit solvent model VASPsol with water permittivity of 78.4 was used to consider the solvation effect⁵⁴. The Cu(111)/Cu₂O(111) model is obtained by deleting some of the O atoms from Cu₂O(111) (a $p(4 \times 2)$ Cu₂O(111) unit cell) and then optimizing the lattice and atomic position. The optimized Cu(111)/Cu₂O(111) has the lattice parameters $a = 21.48 \text{ \AA}$, $b = 10.29 \text{ \AA}$, $c = 23.62 \text{ \AA}$, $\alpha = 90^\circ$, $\beta = 90^\circ$, $\gamma = 118.63^\circ$. The $1 \times 2 \times 1$ k-point mesh set was used for Cu(111)/Cu₂O(111) composite slab models. The Cu₂O(111) model was obtained using a $p(2 \times 2)$ unit cell, and the Cu(111) model was also obtained using a $p(2 \times 2)$ unit cell. To take into account the on-site Coulomb interaction between 3 d electrons of Cu, the GGA + U approach was also employed with a U-J value of 4 eV. Note that Cu(111) does not use GGA + U. The reaction free energy change can be obtained with the equation below:

$$\Delta G = \Delta E + ZPE - T\Delta S \quad (10)$$

where ΔE is the total energy difference before and after intermediate adsorbed, ΔE_{ZPE} and ΔS are, respectively, the differences of zero-point energy and entropy. The zero point energy and entropy of free molecules and adsorbents were obtained from the vibrational frequency calculations. Since VASP cannot precisely describe the charged system, the energy of NO_3^- needs to be measured according to this literature. In addition, the greater the pH value, the more difficult the protonation process. Therefore, it is more important to consider a reasonable pH value to determine the competition reaction. When the PH is introduced, the Gibbs free energy change for all protonation processes is obtained by the following equation:

$$\Delta G_{\text{pH}} = \Delta G + \text{pH} \times k_B T \ln 10 \quad (11)$$

where k_B is the Boltzmann constant, and T is the temperature, here taken as 298.15 K. The pH value used in this article is set to 9. The entire reaction path is determined step by step by selecting the step with the lowest reaction energy among protonation, adsorption, desorption and coupling.

Data availability

Source Data file has been deposited in Figshare under accession code DOI link⁵⁵. The raw data of the figures in the main manuscript are available in figshare with the identifier(s) <https://doi.org/10.6084/m9.figshare.27964467>. All other data needed to evaluate the conclusions in the paper are present in the paper and the Supplementary Information or can be obtained from the corresponding authors upon request. Source data are provided with this paper.

Code availability

The code used in this work can be obtained from the corresponding authors on request.

References

1. Zhang, X. et al. Managing nitrogen for sustainable development. *Nature* **528**, 51–59 (2015).
2. Erismann, J. W. et al. How a century of ammonia synthesis changed the world. *Nat. Geosci.* **1**, 636–639 (2008).
3. Chen, J. et al. Schrock, Beyond fossil fuel-driven nitrogen transformations. *Science* **360**, 6391 (2018).
4. F. M. a. M. P. Francesco Barzagli. From greenhouse gas to feed-stock: formation of ammonium carbamate from CO₂ and NH₃ in organic solvents and its catalytic conversion into urea under mild conditions. *Green Chem.* **13**, 1267–1274 (2011).
5. Service, R. F. Chemistry New recipe produces ammonia from air, water, and sunlight. *Science* **345**, 610–610 (2014).
6. Chen, C. et al. Coupling N₂ and CO₂ in H₂O to synthesize urea under ambient conditions. *Nat. Chem.* **12**, 717–724 (2020).
7. Meng, N. et al. Electrosynthesis of urea from nitrite and CO₂ over oxygen vacancy-rich ZnO porous nanosheets. *Cell Rep. Phys. Sci.* **2**, 100378 (2021).
8. Lv, C. et al. Selective electrocatalytic synthesis of urea with nitrate and carbon dioxide. *Nat. Sustain.* **4**, 868–876 (2021).
9. Geng, J. et al. Ambient electrosynthesis of urea with nitrate and carbon dioxide over iron-based dual-sites. *Angew. Chem. Int. Ed.* **62**, e202210958 (2023).
10. Wei, X. et al. Oxygen vacancy-mediated selective C–N coupling toward electrocatalytic urea synthesis. *J. Am. Chem. Soc.* **144**, 11530–11535 (2022).
11. Zhang, X. et al. Identifying and tailoring C–N coupling site for efficient urea synthesis over diatomic Fe–Ni catalyst. *Nat. Commun.* **13**, 5337 (2022).
12. Yuan, M. et al. Highly selective electroreduction of N₂ and CO₂ to urea over artificial frustrated lewis pairs. *Energy Environ. Sci.* **14**, 6605–6615 (2021).
13. Wang, Y. et al. Nitrate electroreduction: mechanism insight, in situ characterization, performance evaluation, and challenges. *Chem. Soc. Rev.* **50**, 6720–6733 (2021).
14. Chen, W. et al. Unveiling the electrooxidation of urea: Intramolecular coupling of the N–N bond. *Angew. Chem. Int. Ed.* **60**, 7297–7307 (2021).
15. Yuan, M. et al. Unveiling electrochemical urea synthesis by Co-Activation of CO₂ and N₂ with Mott–Schottky heterostructure catalysts. *Angew. Chem. Int. Ed.* **60**, 10910–10918 (2021).
16. Xu, M. et al. Kinetically matched C–N coupling toward efficient urea electrosynthesis enabled on copper single-atom alloy. *Nat. Commun.* **14**, 6994 (2023).
17. Feng, Y. et al. Te-doped Pd nanocrystal for electrochemical urea production by efficiently coupling carbon dioxide reduction with nitrite reduction. *Nano Lett.* **20**, 8282–8289 (2020).
18. Zhu, X. et al. Electrochemical synthesis of urea on MBenes. *Nat. Commun.* **12**, 4080 (2021).
19. Wang, P. et al. Molecular assembled electrocatalyst for highly selective CO₂ fixation to C₂⁺ products. *ACS Nano* **16**, 17021–17032 (2022).
20. Yang, Y. et al. Operando studies reveal active Cu nanograins for CO₂ electroreduction. *Nature* **614**, 262–269 (2023).
21. Yao, K. et al. Mechanistic insights into OC–COH coupling in CO₂ electroreduction on fragmented copper. *J. Am. Chem. Soc.* **144**, 14005–14011 (2022).
22. Zhao, Z. et al. Polydopamine coating of a metal–organic framework with Bi-copper sites for highly selective electroreduction of CO₂ to C₂⁺ products. *ACS Catal.* **12**, 7986–7993 (2022).
23. Zhu, C. et al. Dynamic restructuring of epitaxial Au–Cu biphasic interface for tandem CO₂-to-C₂⁺ alcohol conversion. *Chem.* **8**, 3288–3301 (2022).
24. Zhu, H. et al. A porous π–π stacking framework with dicopper(I) sites and adjacent proton relays for electroreduction of CO₂ to C₂⁺ products. *J. Am. Chem. Soc.* **144**, 13319–13326 (2022).
25. Wei, X. et al. Dynamic reconstitution between copper single atoms and clusters for electrocatalytic urea synthesis. *Adv. Mater.* **35**, 2300020 (2023).
26. Pan, L. et al. Single-atom or dual-atom in TiO₂ nanosheet: Which is the better choice for electrocatalytic urea synthesis? *Angew. Chem. Int. Ed.* **62**, e202216835 (2023).
27. Leverett, J. et al. Tuning the coordination structure of Cu–N–C single atom catalysts for simultaneous electrochemical reduction of CO₂ and NO₃[−] to urea. *Adv. Energy Mater.* **12**, 2201500 (2022).
28. Meng, N. et al. Oxide-derived core–shell Cu@Zn nanowires for urea electrosynthesis from carbon dioxide and nitrate in water. *ACS Nano* **16**, 9095–9104 (2022).
29. Liu, S. et al. AuCu nanofibers for electrosynthesis of urea from carbon dioxide and nitrite. *Cell Rep. Phys. Sci.* **3**, 100869 (2022).
30. Shin, S. et al. Copper with an atomic-scale spacing for efficient electrocatalytic co-reduction of carbon dioxide and nitrate to urea. *Energy Environ. Sci.* **16**, D3EE00008G (2023).
31. Mukherjee, J. et al. Understanding the site-selective electrocatalytic Co-reduction mechanism for green urea synthesis using copper phthalocyanine nanotubes. *Adv. Funct. Mater.* **32**, 2200882 (2022).
32. Li, Z. et al. Magic hybrid structure as multifunctional electrocatalyst surpassing benchmark Pt/C enables practical hydrazine fuel cell integrated with energy-saving H₂ production. *eScience* **2**, 416–427 (2022).
33. Liu, Y. et al. Manipulating dehydrogenation kinetics through dual-doping Co₃N electrode enables highly efficient hydrazine oxidation assisting self-powered H₂ production. *Nat. Commun.* **11**, 1853 (2020).
34. Li, Y. et al. Partially exposed RuP₂ surface in hybrid structure endows its bifunctionality for hydrazine oxidation and hydrogen evolution catalysis. *Sci. Adv.* **6**, eabb4197 (2020).
35. Platzman, I. et al. Oxidation of polycrystalline copper thin films at ambient conditions. *J. Phys. Chem. C* **112**, 1101–1108 (2008).
36. Li, D. et al. Accelerating electron-transfer dynamics by TiO₂-immobilized reversible single-atom copper for enhanced artificial photosynthesis of urea. *Adv. Mater.* **34**, 2207793 (2022).
37. Wang, Y. et al. Unveiling the activity origin of a copper-based electrocatalyst for selective nitrate reduction to ammonia. *Angew. Chem. Int. Ed.* **59**, 5350–5354 (2020).
38. Larson, P. X-Ray Induced photoelectron and auger-spectra of Cu, CuO, Cu₂O, and Cu₂S thin-films. *J. Electron Spectrosc.* **4**, 213–218 (1974).
39. Hu, Y. et al. Fabrication of coral-like Cu₂O nanoelectrode for solar hydrogen generation. *J. Power Sources* **242**, 541–547 (2013).
40. Mao, Y. et al. Electrochemical synthesis of hierarchical Cu₂O stars with enhanced photoelectrochemical properties. *Electrochim. Acta* **62**, 1–7 (2012).
41. Cheng, W. et al. Lattice-strained metal-organic-framework arrays for bifunctional oxygen electrocatalysis. *Nat. Energy* **4**, 115–122 (2019).
42. Zhao, Y. et al. Efficient urea electrosynthesis from carbon dioxide and nitrate via alternating Cu–W bimetallic C–N coupling sites. *Nat. Commun.* **14**, 4491 (2023).
43. Chitsiga, T. et al. Effect of the presence of water-soluble amines on the carbon dioxide (CO₂) adsorption capacity of amine-grafted poly-succinimide (PSI) adsorbent during CO₂ capture. *Energy Procedia* **86**, 90–105 (2016).
44. Manivannan, M. Investigation of inhibitive action of urea–Zn²⁺ system in the corrosion control of carbon steel in sea water. *Int. J. Eng. Sci. Technol.* **3**, 0975–5462 (2011).

45. Zhang, S. et al. High-efficiency electrosynthesis of urea over bacterial cellulose regulated Pd–Cu bimetallic catalyst. *EES Catal.* **1**, 45–53 (2023).
46. Xiao, H. et al. Cu metal embedded in oxidized matrix catalyst to promote CO₂ activation and CO dimerization for electrochemical reduction of CO₂. *Proc. Natl Acad. Sci.* **114**, 6685–6688 (2017).
47. Jiao, D. et al. Mo₂P monolayer as a superior electrocatalyst for urea synthesis from nitrogen and carbon dioxide fixation: a computational study. *Energy Environ. Mater.* **2**, 12496 (2022).
48. Roy, Prodyut et al. Dual-Silicon-Doped Graphitic Carbon Nitride Sheet: An Efficient Metal-Free Electrocatalyst for Urea Synthesis. *J. Phys. Chem. Lett.* **12**, 10837–10844 (2021).
49. Fields, M. et al. Role of subsurface oxygen on Cu surfaces for CO₂ electrochemical reduction. *J. Phys. Chem. C* **122**, 16209–16215 (2018).
50. Liu, X. et al. Mechanism of C–N bonds formation in electrocatalytic urea production revealed by ab initio molecular dynamics simulation. *Nat. Commun.* **13**, 5471 (2022).
51. Yang, G. et al. Gaseous CO₂ coupling with N-Containing intermediates for key C–N bond formation during urea production from coelectrolysis over Cu. *ACS Catal.* **12**, 11494–11504 (2022).
52. Li, H. et al. Ligand engineering towards electrocatalytic urea synthesis on a molecular catalyst. *Nat. Commun.* **15**, 8858 (2024).
53. Wei, J. et al. Constructing Co@C nanoparticles with chainmail-structure for highly efficient hydroformylation of 1-hexene. *Chem. Eng. J.* **492**, 151963 (2024).
54. Mathew, K. et al. Implicit Solvation Model for Density-Functional Study of Nanocrystal Surfaces and Reaction Pathways. *J. Chem. Phys.* **140**, 084106 (2014).
55. Dai, Z. et al. Surface Engineering on bulk Cu₂O for efficient electrosynthesis of Urea, Figshare, <https://doi.org/10.6084/m9.figshare.27964467> (2025).

Acknowledgements

G.Q.Z. acknowledges the National Natural Science Foundation of China (Grant No. 52072359), the Recruitment Program of Global Experts and the Fundamental Research Funds for the Central Universities (WK2060000016). The numerical calculations in this paper have been done in the Supercomputing Center of University of Science and Technology of China. The authors are grateful to infrared beamline (BL01B) at NSRL for the experimental beamtime support. This work was partially carried out at the Instruments Center for Physical Science, University of Science and Technology of China.

Author contributions

Z.C.D., and G.Q.Z. contributed to the conception of the study. Z.C.D. performed the experiments. Y.X.C. conducted the Density Functional

Theory (DFT) calculations analysis. H.K.Z. provided assistance with the Scanning Electron Microscope (SEM) analysis and assisted with the electrochemical in situ Fourier Transform Infrared (FTIR) spectroscopy analysis. M.Y.C., B.C.Z., P.Y.F., and Y.F.F. provided help in the experimental part. G.Q.Z. contributed significantly to the analysis and manuscript preparation. The project was supervised by G.Q.Z. All authors participated in the analysis with constructive discussions.

Competing interests

The authors declare no competing interests.

Additional information

Supplementary information The online version contains supplementary material available at <https://doi.org/10.1038/s41467-025-57708-7>.

Correspondence and requests for materials should be addressed to Genqiang Zhang.

Peer review information *Nature Communications* thanks Pranab Sarkar and the other anonymous reviewers for their contribution to the peer review of this work. A peer review file is available.

Reprints and permissions information is available at <http://www.nature.com/reprints>

Publisher's note Springer Nature remains neutral with regard to jurisdictional claims in published maps and institutional affiliations.

Open Access This article is licensed under a Creative Commons Attribution-NonCommercial-NoDerivatives 4.0 International License, which permits any non-commercial use, sharing, distribution and reproduction in any medium or format, as long as you give appropriate credit to the original author(s) and the source, provide a link to the Creative Commons licence, and indicate if you modified the licensed material. You do not have permission under this licence to share adapted material derived from this article or parts of it. The images or other third party material in this article are included in the article's Creative Commons licence, unless indicated otherwise in a credit line to the material. If material is not included in the article's Creative Commons licence and your intended use is not permitted by statutory regulation or exceeds the permitted use, you will need to obtain permission directly from the copyright holder. To view a copy of this licence, visit <http://creativecommons.org/licenses/by-nc-nd/4.0/>.

© The Author(s) 2025